Role of the preheating temperature during electron beam powder bed fusion (PBF-EB/M) in precipitation of ’ and carbides in Inconel 738 superalloy

Journal of Materials Research and Technology 37 (2025) 4639–4650

Contents lists available at ScienceDirect

Journal of Materials Research and Technology

journal homepage: www.elsevier.com/locate/jmrt

Role of the preheating temperature during electron beam powder bed fusion (PBF-EB/M) in precipitation of γ' and carbides in Inconel 738 superalloy

S. Lerda [a,*], B. Luo [b], G. Marchese [a,c], X. Zhao [b], S. Biamino [a,c], S. Dadbakhsh [b]

[a] Department of Applied Science and Technology (DISAT), Politecnico di Torino, Corso Duca degli Abruzzi 24, 10129, Torino, Italy
[b] Production Engineering Department, KTH Royal Institute of Technology, Brinellvagen 68, 11428, Stockholm, Sweden
[c] Consorzio Interuniversitario Nazionale per la Scienza e Tecnologia dei Materiali (INSTM), Via G. Giusti 9, 50121, Firenze, Italy

ARTICLE INFO

Keywords:
Ni-based superalloys
Inconel 738
Electron beam powder bed fusion
Preheating temperature
Gamma prime

ABSTRACT

In this work, two tailored electron beam powder bed fusion (PBF-EB/M) preheating conditions were selected to build Inconel 738 (IN738) superalloy. The IN738 samples produced at 1025 °C (R1) and 950 °C (R2) were characterized in the as-built condition to investigate the effect of the preheating temperature on the evolution of their microstructural features. Both samples showed low residual porosity (<0.2 %), and the microstructure displayed columnar grains elongated in the building direction, together with the precipitation of γ' (Ni_3Al), Ta-rich MC, and Cr-rich $M_{23}C_6$. The R1 condition developed a multimodal γ′ size distribution subjected to strong coarsening along the building direction. This scenario provoked a notable microhardness gradient and micro-crack formation due to the severe residual stresses developed. On the contrary, the lower preheating temperature chosen for the R2 condition provoked the precipitation of γ′ in a homogeneous monomodal size distribution with negligible coarsening along the building direction, thus lowering the residual stresses (no micro-cracks) and stabilizing the microhardness. The preheating temperature thus had a lower impact on carbide precipitation and evolution compared to the γ' one. Both conditions experienced the precipitation of Cr-rich $M_{23}C_6$ and Ta-rich MC carbides along the grain boundaries, coupled with fine Ta-rich MC carbide precipitation inside the grains. However, the R2 condition underwent slightly lower precipitation. The current study therefore highlights the beneficial effects of tailoring the PBF-EB/M preheating temperature to control the evolution of the microstructural features and their effect on the development of residual stresses and microhardness stabilization in the as-built condition.

1. Introduction

The electron beam powder bed fusion process (PBF-EB/M) is an additive manufacturing (AM) technology that allows the building of parts layer by layer, providing a preheating step before selective melting. This additional preheating represents a unique challenging step among other AM technologies, helping to improve the process stability [1]. Preheating the powder bed allows the consolidation of powder particles, thereby preventing the undesired smoke phenomena that occur with severe powder spreading, which often leads to building failures [2,3]. Moreover, the presence of a preheating step can increase the process temperatures between 700 °C and 1100 °C [4], drastically reducing the residual stress development during the building. This approach maximizes the processability of crack-sensitive alloys, such as Ni-based superalloys, compared to other AM techniques [5,6].

Ni-based superalloys are widely studied for their high-temperature performance, particularly those with high percentages of strengthening gamma prime (γ', $Ni_3(Al, Ti)$) phase (from 40 vol% to 80 vol%) [7,8]. These alloys show excellent thermal fatigue resistance, corrosion resistance, and good mechanical properties up to 1000 °C [9,10]. Consequently, these materials are predominantly used in the aerospace industry [11].

Inconel 738 (IN738) represents a valuable example since it is classified as a γ′ precipitation-strengthened Ni-based superalloy. Below 1175 °C, Ni, Al, and Ti form a coherent cubic γ′ phase, considered the most effective strengthening phase in Ni-based superalloys. The γ′ can

* Corresponding author. Corso Duca degli Abruzzi 24, 10129, Torino, Italy.
E-mail address: serena.lerda@polito.it (S. Lerda).

https://doi.org/10.1016/j.jmrt.2025.07.092
Received 27 March 2025; Received in revised form 8 July 2025; Accepted 9 July 2025
Available online 11 July 2025

assume three different shapes depending on the mismatch with the γ matrix. Spherical γ' precipitates form with low mismatches (0–0.2), minimizing surface energy. Higher mismatches (0.5–1.0) lead to cuboidal precipitates, while mismatches exceeding 1.25 result in plate-like precipitates. Additionally, carbides can contribute as strengthening phases in Ni-based superalloys. For instance, Ta, Ti, and Hf combined with C can precipitate as primary MC carbides during solidification, which subsequently decompose into $M_{23}C_6$ (Cr-rich) between 700 °C and 1000 °C, and M_6C (Mo, W-rich) between 815 °C and 980 °C [10,11].

IN738 was traditionally produced by casting technology [12,13], which results in a highly segregated matrix with detrimental γ/γ' eutectic formation, reducing the thermal stability of the alloy. Moreover, the high hardness of IN738 drastically reduces its machinability, resulting in severe heat formation during subtractive manufacturing [14–16]. The combination of these factors led to an increasing interest in the processability of IN738 through PBF-EB/M technologies [7,17–20]. Moreover, the high-temperature PBF-EB/M conditions make it a valuable candidate for strain-age-sensitive IN738 production [21–23].

PBF-EB/M was then used to build IN738 samples, leading to the evaluations of the microstructural evolution. For instance, Haghdadi et al. [24] investigated the microstructure of the as-built condition. The microstructural characterization focused on the in situ precipitation of γ′ during the PBF-EB/M process, rarely observed in laser powder bed fused (PBF-LB/M) IN738 [25]. The preheating temperature above 1000 °C enabled homogeneous γ′ precipitation with a multimodal size distribution. The measurements reported a first population ranging between 400 nm and 600 nm and a second one from 5 nm to 50 nm. This study highlighted for the first time the capability of PBF-EB/M to induce an in-situ precipitation of γ′ phase. Later, Lim et al. [26] focused on the microstructural and property gradient investigations along the building direction. The evaluation was based on the decreasing soaking times experienced during the growth of the sample. The work correlated the increase in elastic modulus and hardness that occurred along the building direction with the γ' size reduction. Finally, Li et al. [27] compared the as-built and heat-treated PBF-EB/M IN738 with the cast ones. In this case, a preheating temperature of 1070 °C was set to minimize the temperature gradient. The elongated grains detected in the as-built PBF-EB/M IN738 strengthened the alloy compared to the cast condition. Moreover, the study analyzed the effect of hot isostatic pressing (HIP) and heat treatment on the PBF-EB/M IN738 microstructure and mechanical properties. The combined impact of pore reduction and microstructural changes induced by HIP led to an increase in the elongation ratio, while the subsequent full heat treatment allowed a further yield and ultimate strength increase.

So far, literature reports successful building and characterization of as-built PBF-EB/M IN738 samples. However, it would be additionally interesting to investigate the effect of preheating temperature and its influence on the evolution of IN738 phases, such as γ' and carbides.

The current work investigates the realization and the potential differences of IN738 samples made at two different preheating temperatures: 1025 °C and 950 °C. The 1025 °C condition fitted with the literature suggested preheating interval. On the contrary, the 950 °C aimed to minimize the precipitation and growth of the IN738 main phases. Microstructure and phase precipitation were investigated in the two conditions, and their evolution correlated with the preheating temperature. In addition, density measurements, deep microstructural investigations, and microhardness evaluation were performed to fully characterize the as-built samples. The result underlined the impact of the preheating temperature on the microstructural features development of PBF-EB/M IN738. A lower preheating temperature allowed a more controlled precipitation of γ' and carbides, thus reducing the microstructural and property gradient along the building direction.

2. Materials and methods

2.1. Powder characterization

Gas-atomized IN738 powders were purchased from LPW, UK (now part of Carpenter Additive) with a diameter range of 44–106 μm. Before processing, the IN738 powder batch was sieved below 105 μm with an automatic sieving system. The chemical composition and morphology of IN738 powder were analyzed using a scanning electron microscope (SEM, Phenom ProX, Phenom-World, Eindhoven, The Netherlands), with an energy dispersive spectroscopy (EDS) system. Moreover, the C content was evaluated by a LECO detector (LECO, CS 744 LECO-analyzer, Leco, St. Joseph, MI, USA). Table 1 reports the chemical composition in wt.% for the main alloying elements of IN738.

Fig. 1 a reports a low-magnification SEM image of the powder particles' batch. The IN738 powder was mainly composed of spherical particles with sporadic satellites that did not affect the powder spreadability during the PBF-EB\M. The cross-section powder microstructure (Fig. 1 b) was revealed to have a cellular structure due to the rapid cooling undergone by the gas-atomization process.

2.2. Thermal phase transformation investigation

A differential scanning calorimetry analysis was performed using a DSC Setaram TGA 92 16.18 (Setaram Kep Technologies, Sophia Antipolis, France) to investigate the precipitation of γ' during the cooling step after melting. A 20 K/min heating rate was used to heat the sample to 1400 °C, inducing melting, while the cooling evolution at 20 K/min was recorded from 1400 °C to 600 °C.

Thermo-Calc software simulated the $M_{23}C_6$ carbide Time Temperature Transformation (TTT) curve in the simplified mode [28]. The commercial CALCPHAD database for Ni-based alloys (TCNI8/Ni superalloys) provided thermodynamic information, while the mobility and diffusion information were taken from the NIST Ni superalloys database. The IN738 chemical composition used in the simulation is reported in Table 1.

2.3. PBF-EB/M production

Cuboid samples were built using an A2X Arcam PBF-EB/M machine (made by Arcam, Sweden, now called Colibrium Additive, a GE Aerospace company) with a retrofitted platform and an accelerating voltage of 60 kV. The R1 condition was set at a preheating temperature of 1025 °C according to the interval identified by the literature [24,26], while the R2 preheating temperature was set at 950 °C to minimize the phase's precipitation and growth. To enable preheating at a lower temperature of R2, a completely new set of optimal parameters was developed and implemented to reach dense parts. Obtaining 950 °C with the R1 preheating condition would have meant reducing the repetitions, thus affecting the powder sintering capability, and increasing the risk of smoke phenomena [29]. Table 2 shows the parameters used to reach dense parts at the R1 and R2 preheating conditions. To do so, defocused beams to preheat the powder layer of 75 μm have been used. The preheating temperature was measured by a thermocouple located below the building platform throughout the entire building.

The melting parameters were optimized separately for the R1 and R2 conditions; the R1 was applied using a single-step melting, while the R2 melting underwent a two-step melting to ensure powder consolidation. The first step used a defocused beam (FO = −10 mA) while the second melting was performed using a focused beam (FO = 17 mA). This was developed according to the knowledge and experience of the researchers from previous works [29,30]. It should be noted that a scanning strategy with a rotation of 90° was used between consecutive layers for both cases.

Table 1
IN738 chemical composition in wt.% evaluated with EDS and LECO combustion analysis.

Ni	Cr	Co	Al	Ta	Hf	Mo	Nb	Ti	Fe	Mn	C
Bal.	14.9	4.6	4.1	6.2	3.4	0.2	0.2	0.02	0.02	0.02	0.1

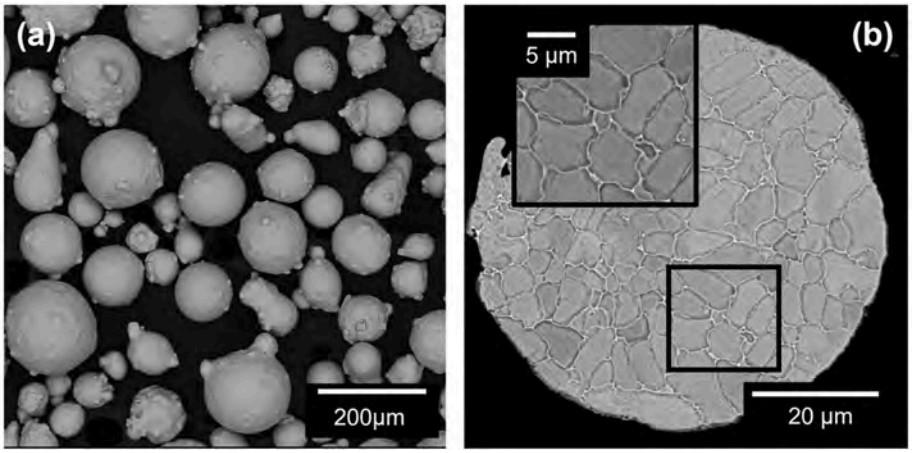

Fig. 1. (a) SEM low-magnification image showing a representative IN738 batch of powder particles. (b) SEM image of an IN738 cross-section particle with the reference microstructure.

Table 2
Arcam A2X process parameters used to manufacture IN738 parts in the R1 and R2 conditions.

Parameter	R1-Preheating	R2-Preheating	Parameter	R1-Melting	R2-Melting 1	R2-Melting 2
Preheating Temp.	1025 °C	950 °C	**Energy density**	21 J/mm^3	14 J/mm^3	58 J/mm^3
Beam current	48 mA	11 mA	**Beam current**	15 mA	5.5 mA	11 mA
Beam speed	15750 mm/s	8000 mm/s	**Beam speed**	4530 mm/s	3000 mm/s	3000 mm/s
Line offset	1 mm	1 mm	**Line offset**	0.125 mm	0.1 mm	0.1 mm
Focus offset (FO)	425 mA	−10 mA	**Focus offset (FO)**	15 mA	−10 mA	17 mA

2.4. Microstructural characterization

The R1 and R2 cubes with dimensions 10 x 10 x 10 mm^3 were characterized in the as-built (AB) condition. Cubes were cut along the building direction (z), ground with SiC papers, and polished up to 1 μm diamond suspension. The residual porosity was evaluated in both conditions using a light optical microscope (LOM, Leica DMI5000 M, Wetzlar, Germany). 20 images at 50x magnification were acquired and then analyzed through ImageJ software.

An additional polishing step with a silica suspension (0.04 μm) was performed for the observations with a focused ion beam scanning electron microscope (FIB-SEM) (TESCAN S9000G, Tescan Company, Brno, Czech Republic) equipped with an electron backscattered diffraction (EBSD) detector. The EBSD analysis was performed by scanning samples at 20 kV and 10 nA using a step size of around 3.8 μm with a tilting angle of 70°. The grain reference orientation deviation (GROD) and kernel average misorientation (KAM) maps were evaluated to reveal the residual stresses in the microstructure. The GROD map displays the misorientation of a point within a reference value in a grain, while the KAM maps and curves report the average misorientation between neighbour points [31]. Moreover, low-angle grain boundaries (LAGBs) and high-angle grain boundaries (HAGBs) were evaluated.

Microstructural investigations were carried out using LOM and SEM (Zeiss EVO 15, Carl Zeiss AG, Jena, Germany), equipped with an EDS probe (Ultim-max, Oxford instruments), moreover, the R1 and R2 samples were etched with Kalling's No.2 solution for 7 s to reveal the general microstructure and electrochemically etched with orthophosphoric acid (20 vol%) for 5 s to highlight γ' precipitates, according to ASTM E407-07. The phase identification was performed by means of EDS analyses for both R1 and R2 with a particular focus on the grain boundary area. The microstructure was investigated along the building direction, focusing on three different areas. The bottom, which stands closer to the building platform with a higher soaking time at the preheating temperature, the middle, and the top of the samples, which respectively underwent a shorter soaking time. The γ' quantification and size measurement involved the post-processing of 5 SEM images for each area at 20000X, 50000X, and 100000X magnification with ImageJ software for both R1 and R2 samples. Similarly, the carbides fraction and dimension were evaluated by post-processing 5 SEM images at 5000X for each area, for R1 and R2 using ImageJ software. The different contrast of back-scattered SEM images makes it possible to highlight the carbides from the matrix, allowing their evaluation. Finally, the crack characterization of R1 samples was performed with SEM analyses.

2.5. Microhardness characterization

The Vickers microhardness (HV) test was carried out on the R1 and R2 samples. The microhardness test was performed with a DHV-1000 digital micro durometer (HUATEC Group Corporation, Beijing, China) using 200 gf and 15 s dwell following the ASTM E92-23 [32]. Three indentations for each zone (bottom, middle, and top) were performed. The reported result for each zone represents a mean value among the three indentations.

3. Results and discussion

3.1. Preheating temperature selection

Fig. 2 a represents a DSC heating (orange) and cooling (green) curve of IN738. The sample melted during the heating step, and the cooling curve was considered to identify the precipitation behaviour. Starting from the high temperature (indicated by the green curve), the exothermic peak at 1380 °C was identified as the onset of γ matrix solidification. After that first transformation, two other main exothermic peaks were identified, respectively at the temperature onset of 1335 °C and 1050 °C. The 1335 °C one was attributed to MC precipitation, while the 1050 °C one was recognized as the γ′ precipitation [17,33]. The MC carbides are also known as high-temperature carbides, and their precipitation was found to occur right after the γ solidification [10]. Therefore, the preheating temperature ranges (700 °C–1100 °C) might have a side effect on MC precipitation and growth. Consequently, in this work, the MC carbides were not considered for the two preheating temperature setup choices. Instead, γ′ was used as the main reference due to its strong influence on the crack subjectivity of Ni-based superalloys [9]. The R1 condition was identified at 1025 °C, fitting the temperature interval of the γ′ precipitation peak. According to the literature [24,26,27], preheating temperatures above 1000 °C guaranteed the γ′ precipitation, justifying the R1 condition choice. Conversely, the R2 choice was set at 950 °C, this approach could increase the cooling rates toward the maximum γ' precipitation range, thus limiting its precipitation and growth.

To further investigate the two preheating temperature selections, the $M_{23}C_6$ carbides temperature evolution was studied using TTT curve simulation by Thermo-Calc software. The results are visible in Fig. 2 b. According to the curve, the temperature range of $M_{23}C_6$ precipitation stood below 1100 °C, which fitted with the outcomes reported by Tancret et al. [34]. Therefore, their presence could not theoretically be avoided during the building step. The TTT curve displayed a preferential $M_{23}C_6$ precipitation around 1025 °C, where slightly more than 1 h soaking guaranteed the precipitation of carbides. Lowering the preheating temperature to 950 °C could increase this time to trigger the $M_{23}C_6$ precipitation. In this way, the formation of $M_{23}C_6$ carbides could be slowed down, thus minimizing their presence in the matrix.

Based on these results, the R1 (1025 °C) was chosen to represent the maximum precipitation condition, while the R2 (950 °C) was set to a slightly lower temperature to achieve a lower precipitation rate, allowing for a comparison of the material properties at different precipitation kinetics.

3.2. Porosity and phases identification

Fig. 3 a and b represent an example of cross-sectional images of AB R1 and R2. As seen, in both cases of the R1 and R2 IN738 samples, the residual porosity was well below 0.2 %. The defects mainly included spherical gas porosities with diameters below 50 μm. Despite the two different preheating setups, the separate melting optimization allowed for reaching similar levels of residual porosity. The result highlighted the possibility of obtaining dense samples at both 1025 °C and 950 °C, thanks to tailored melting parameters.

After the porosity evaluation, the grain structure was investigated at low magnification. The LOM images are reported in Fig. 4 a and b for the R1 and R2 samples. The images reported the scenario evolution for both samples along the building direction. The general microstructure of AB R1 and R2 was composed of columnar grains elongated in the building direction, which grew for more than one layer. The grain size for R1 and R2 ranged in the same interval. The average width of grains was found to lie between 110 μm and 130 μm, while the average length stood between less than 1 mm to several mm, as displayed in Fig. 4. The use of differential preheating temperature did not drastically influence the grain size evolution along the building direction. In both cases, the epitaxial growth typical of AM products was identified. The grain growth along the building direction can be explained by the preferential heat dissipation from the core to the top edge of the samples [35,36]. It is interesting to note that the negligible influence of the preheating temperature on grain distribution was already reported in the literature for PBF-EB/M IN718 [37]. The authors observed comparable grain structures in the IN718 samples processed at 1000 °C and 950 °C preheating temperatures, confirming that this parameter has a negligible effect on grain morphology.

Fig. 5 a and b show the low magnification SEM images and EDS map of the R1 and R2 conditions. The images and maps are focused on a grain boundary area to highlight and identify the microstructural features.

The R1 condition (Fig. 5 a) revealed the presence of two main precipitates soaked in the γ matrix and along the grain boundaries. The first type of phase revealed a bright tone with globular to blocky shapes and precipitation inside grains and along the grain boundaries. The EDS found them enriched in Ta and C, letting their identification as high-temperature Ta-rich MC carbides [38,39]. The second species was observed to have a dark shade and globular to elongated shape, located only along the grain boundaries. Their distribution was found non-homogeneous, and the EDS analyses highlighted higher concentrations of Cr and C, thus indicating the association with $M_{23}C_6$ carbides [38–40]. Similarly, the R2 sample (Fig. 5 b) revealed the presence of two main species along the grain boundaries and inside the grain area. Both

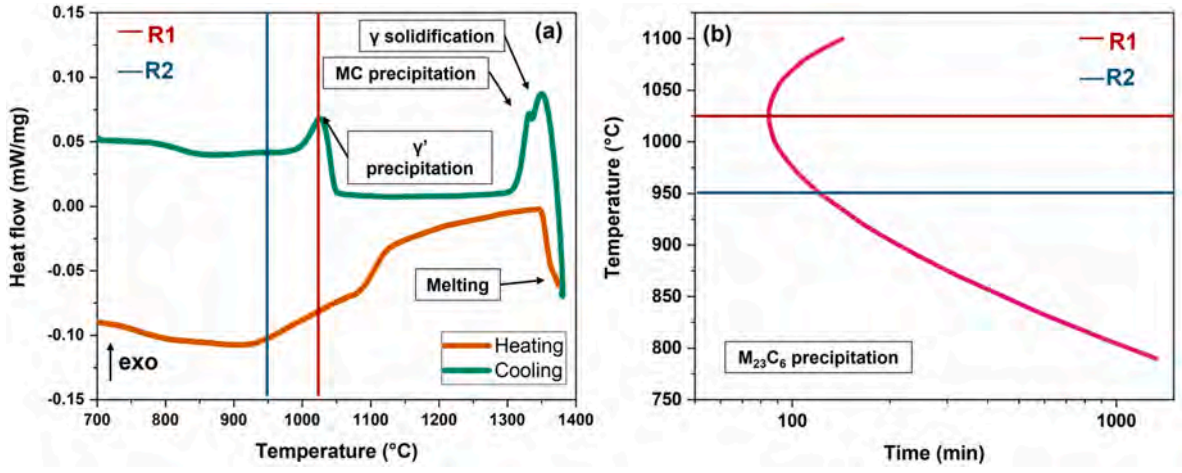

Fig. 2. (a) The DSC heating (orange) and cooling (green) curves of IN738. The precipitation was investigated in the cooling step after the superalloy melting in the heating one. (b) Thermo-Calc simulation of the TTT curve for the precipitation of $M_{23}C_6$ carbide at the grain boundary in IN738 superalloy.

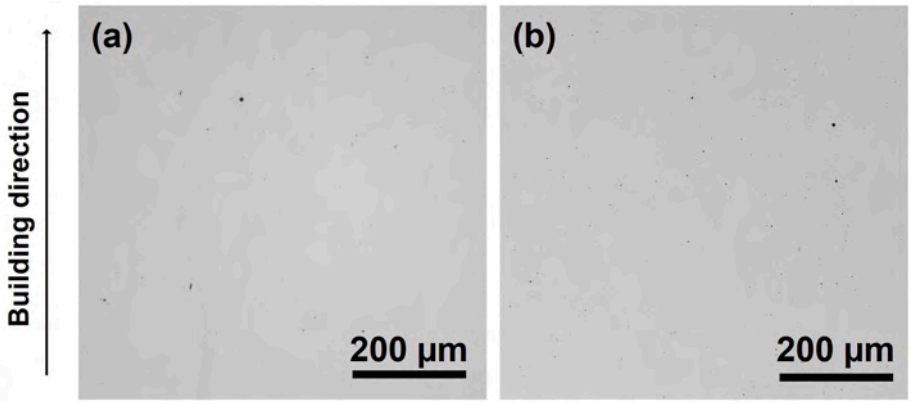

Fig. 3. Cross-section LOM images acquired along the building direction of a polished (a) R1 and (b) R2 samples.

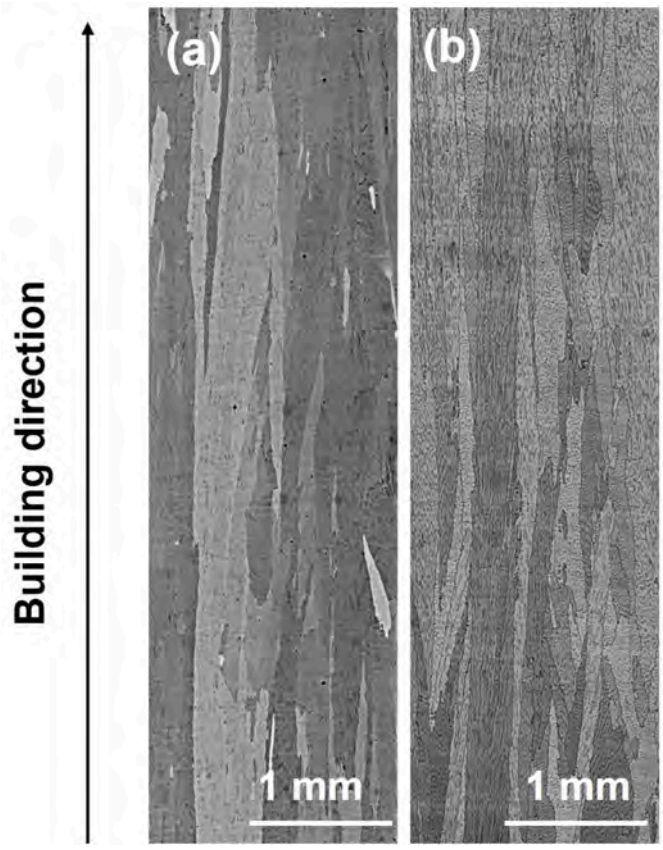

Fig. 4. Cross-section LOM images acquired along the building direction of a chemical etched (a) R1 and (b) R2 samples.

types of carbides found in the R1 sample were detected in the R2 one. The Ta-rich MC carbides were observed along the grain boundaries and inside grains with shapes and distributions close to the R1 condition. On the other hand, the Cr-rich $M_{23}C_6$ carbides were rarely found with globular and elongated shapes decorating a few grain boundaries.

By comparing the two scenarios, the temperature proved to have a limited role in the type of phases observed. This assessment is supported by the literature on IN718, which reports the precipitation of similar microstructural features at preheating temperatures of 950 °C and 1000 °C [37]. In the current work, the preheating temperature had a negligible effect on MC carbide precipitation, leading to the detection in both R1 and R2 samples. The presence of MC carbides in the AB condition has already been reported in other literature works [24,26,27]. The $M_{23}C_6$ carbides underwent limited precipitation in both cases; however, reducing the preheating temperature allowed for a further decrease in the concentration, approaching total absence. The results agreed with the TTT diagram reported in Fig. 2 b. The presence of $M_{23}C_6$ could be derived from the transformation of MC carbides [10] or directly precipitate from the matrix in the area of coexistence in the equilibrium diagram [34].

Fig. 5 c and 5 d display the high magnification images of the R1 and R2 conditions inside the grain area. The observation of the R1 sample (Fig. 5 c) revealed a third phase with a multimodal distribution; the coarse particles showed a spherical to cuboidal shape, while the fine population developed a spherical shape with sub-micrometer dimensions. The shape and the distribution inside the γ matrix allowed their identification as γ′ particles [38,39]. Likewise, high-magnification images inside the R2 sample grains zone (Fig. 5 d) highlighted a population of fine and spherical γ′ particles soaked in the γ matrix. The presence of a low thermal gradient during the PBF-EB/M cooling provided enough driving force and time for γ′ precipitation [41]. The higher preheating temperature experienced by the R1 condition could have favored the development of multimodal precipitation of γ'. Despite the hypothesis suggested by the DSC (Fig. 2 a), the γ′ phase was also observed in the R2 condition. Even if the solidification gradient undergone by R2 was more severe compared to the R1 condition, the driving force given was found sufficient to trigger the precipitation of γ', resulting in a fine population development [42].

The phases discussed above will be deeply quantified in terms of fractions and sizes in the following sections.

3.3. Microstructural features evolution

A deeper evaluation of γ' and carbides fraction, as well as their dimensions, was performed to illustrate the effect of the preheating temperature on their evolution. The different soaking times undergone by the samples bottom, middle, and top areas were deepened by evaluating the microstructural features in all three zones.

The γ' evolution in the bottom, middle, and top zones is reported in Fig. 6 for the R1 and R2 samples.

Fig. 6 a–c displays the R1 size and morphology at the top, middle, and bottom zones, respectively. In all the areas, γ′ growth was verified, and two families could be observed, one with globular to cuboidal shape and the other predominantly globular (Figure A1). The first family displayed coarser dimensions with a non-homogeneous distribution, while the second precipitated homogeneously with narrower dimensions in the matrix among the first family of γ′ precipitates. A similar behavior of the γ′ distribution was reported by Haghdadi et al. [24] and Lim et al. [26] in two separate works. The two studies agreed on the definition of the coarse γ′ particles as primary γ′, while the finer ones were defined as secondary γ'. The precipitation was found to occur in two separate

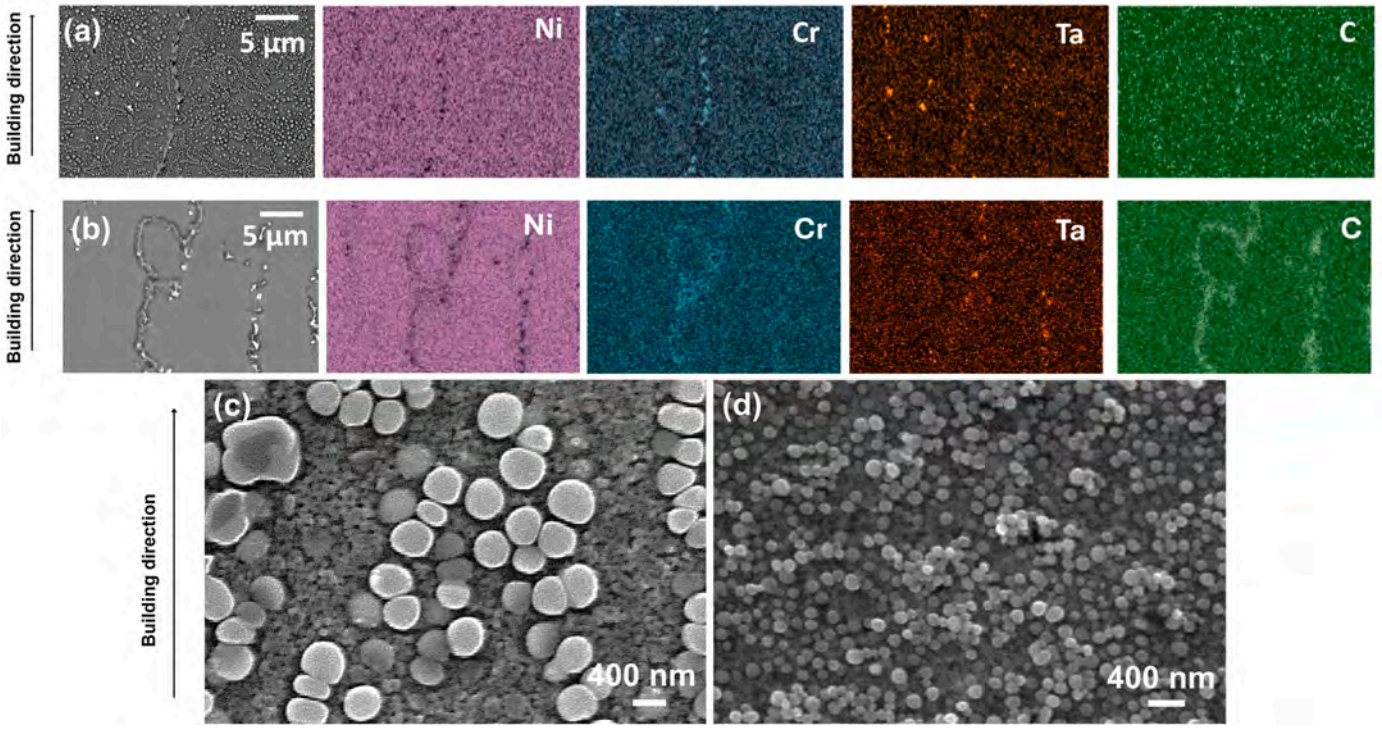

Fig. 5. Cross-section SEM images and EDS maps acquired along the building direction of chemical etched (a) R1 and (b) R2 samples. The images and maps highlight the microstructural features in a grain boundary area. Cross-section SEM images at high magnification on chemical etched (c) R1 and (d) R2 samples. The images highlight the microstructural features inside the grain area.

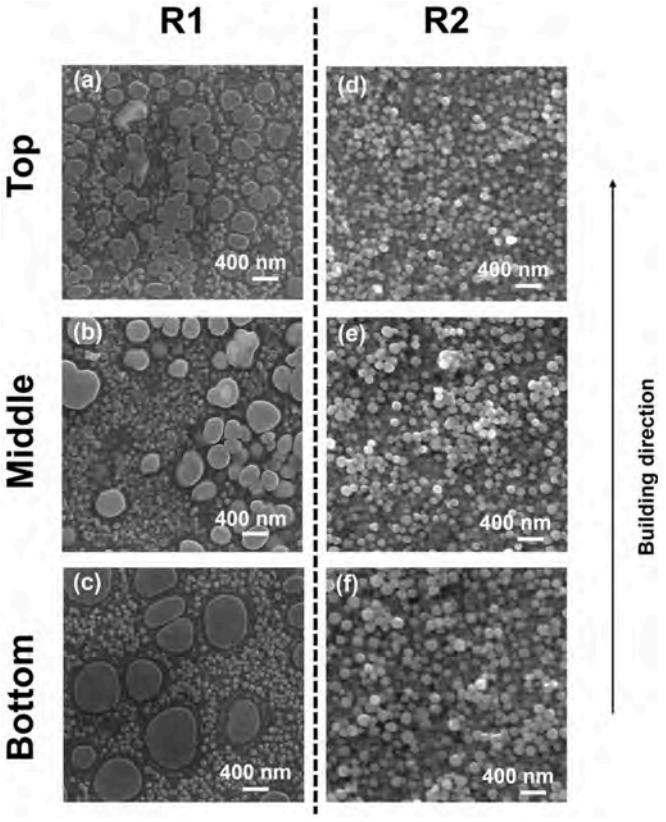

Fig. 6. Cross-section SEM images at high magnification on chemical etched (a, b, c) R1 and (d, e, f) R2 samples. The images show the γ′ evolution inside the grain area at the top (a, d), the middle (b, e), and the bottom (c, f) zones.

stages during the PBF-EB/M process. This could be interpreted according to Radis et al. [42], where the temperature gradient from the melting to the preheating step allowed the precipitation and growth of the primary γ′ phase from the Al and Ti segregated zone. Afterward, the preheating temperature above 1000 °C allowed the dissolution of some primary γ′ particles that further reprecipitated as fine secondary γ' particles during the final cooling step. This complex precipitation path justified the multimodal distribution experienced in the R1 condition.

Fig. 6 d–f display the high magnification scenario at the top, middle, and bottom zones for the R2 sample. The γ′ precipitation occurred homogeneously inside the grains with a unimodal distribution in the bottom, middle, and top areas. By comparing the R2 sample scenario with the R1, the more severe solidification gradient could have pushed the nucleation instead of growth, thus resulting in a finer primary γ′ population [43]. Furthermore, the preheating temperature at R2 might have hindered the γ' dissolution plus reprecipitation behaviour observed in the R1 sample, leading to an unimodal distribution.

Coupled with the shape and distribution evaluation, γ' fraction and dimension were calculated in the bottom, middle, and top areas for the R1 and R2 conditions. Fig. 7 a and b show the results obtained.

Fig. 7 a reports the γ′ fraction evolution along the building direction for the R1 and R2 conditions. R1 revealed a mean γ′ fraction slightly higher than R2, ranging between 55 % to 62 % and 52 % – 55 % respectively. However, by considering the standard deviation, the preheating temperature proved to have a side effect on the amount of γ' precipitated. Overall, the values were found to be in line with the literature [26,27]. Likewise, both conditions underwent a similar evolution along the building direction with a controlled fraction reduction from the bottom to the top of the R1 and R2 samples.

Coupled with the fraction, Fig. 7 b represents the evolution of γ′ size along the building direction for R1 and R2 samples. The primary γ′ size in the R1 sample ranged between 1080 nm and 140 nm, and a severe coarsening was observed descending from the top to the bottom region, with a maximum size going from 850 nm to 1080 nm. Secondary γ′ covered sizes between 89 nm and 30 nm without a sensible size gradient

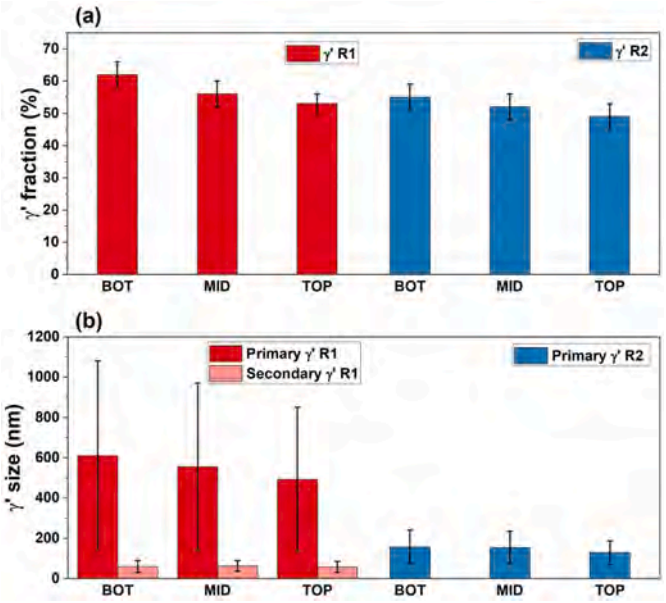

Fig. 7. The fraction (a) and size (b) quantification for the γ′ particles in the R1 and R2 conditions. The graphs report the evolution along the building direction.

along the building direction. The R2 sample displayed primary γ' diameters between 240 nm and 70 nm, with a slight coarsening going toward the bottom of the sample.

By comparing the R1 and R2 conditions, the differences in γ′ size could be attributed to the different thermal histories and evolution undergone by the phase in the two preheating conditions. The result highlighted a more severe microstructural gradient in the R1 sample compared to the R2 one. This behaviour could be justified by the coarsening and coalescence undergone by the γ′ phase during the soaking at a temperature around and above 1000 °C, as reported in the literature [44]. Moreover, the wide nucleation that occurred in the R2 condition, coupled with the dissolution hindering, could have minimized the γ' growth during soaking at 950 °C [42,43].

Coupled with the γ' evolution, the carbides fraction and dimensions were investigated. Fig. 8 shows the evolution of MC and $M_{23}C_6$ carbides in the top, middle, and bottom zones for the R1 (Fig. 8 a–c) and R2 (Fig. 8 d–f) conditions. Despite the differences in preheating conditions, the samples shared similarities in the location and distribution of carbides. MC-type was found abundant and preferentially located inside grains; however, its presence was also detected along the grain boundaries for both R1 and R2 conditions. The MC carbide evolution along the building direction followed similar behaviour for R1 and R2. It involved differences based on the location of MC carbides along the building direction rather than on their fraction and dimension. The MC carbides inside grains underwent a negligible transformation; instead, the grain boundary MC carbides strongly reduced their presence going from the top to the bottom of the samples. Meanwhile, $M_{23}C_6$-type was found only along the grain boundary and generally assembled in clusters. However, their presence was modest in both R1 and R2 samples except for some highly segregated areas preferentially located in the bottom areas of the R1 and R2 samples (Fig. 8 c and f).

The literature confirms the presence of MC carbides in the AB condition, reporting a similar scenario in other PBF-EB/M IN738 [24,26,27]. Moreover, their stability in the temperature ranges studied was also highlighted in similar Ni-based superalloys production by PBF-EB/M IN738 [37]. On the contrary, the presence of $M_{23}C_6$ carbides has not been previously identified in AB IN738 processed by the PBF-EB/M process. In any case, both preheating temperatures used in this work fitted the interval of MC decomposition toward $M_{23}C_6$ verified for Ni-based superalloys [45,46]. This implies the beginning of MC

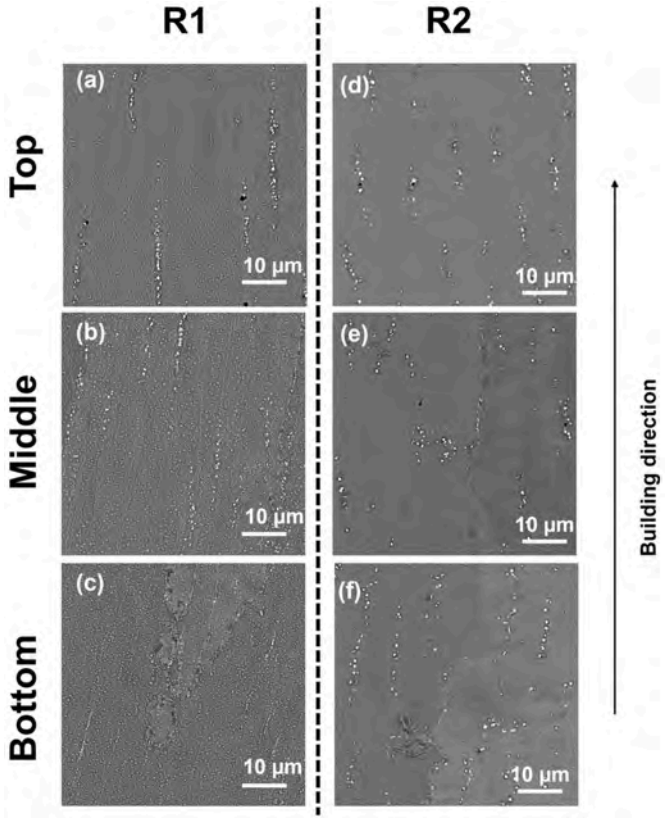

Fig. 8. Cross-section SEM images of chemical etched (a, b, c) R1 and (d, e, f) R2 samples. The images report the carbide evolution at the top (a, d), the middle (b, e), and the bottom (c, f) zones.

decomposition during soaking at preheating temperatures. Moreover, Li et al. [27] identified a temperature threshold to induce $M_{23}C_6$ precipitation for IN738 alloy at 1029 °C, thus justifying their presence in both R1 and R2 conditions. Similar inconsistencies could be found in the AB PBF-LB/M IN738, where Zhou et al. [47] did not report the presence of $M_{23}C_6$ carbide, while Jena et al. [7] observed $M_{23}C_6$ precipitation and ascribed their presence to the interaction between Cr and free C not involved in MC precipitation.

The fraction and dimension of the two carbide types were calculated along the building direction for R1 and R2 conditions (see Fig. 9). Accordingly, Fig. 9 a shows the MC (darker colors) and $M_{23}C_6$ (brighter colors) fraction evolution in the bottom, middle, and top zones for R1 and R2 conditions. R1 underwent a more severe evolution compared to R2; the MC ranged from a fraction of 1.4 % in the top zone to a minimum of 0.4 % in the bottom zone. In the R2 conditions, the MC fraction ranged between 0.9 % in the top area and 0.4 % in the bottom one. In both conditions, the MC carbides fraction observed in the R1 and R2 samples was aligned with the literature [24,26,27]. The $M_{23}C_6$ carbides underwent an opposite evolution along the building direction, displaying a smaller fraction compared to the MC. In the R1 samples, the mean values ranged between 0.2 % in the top zone toward 0.4 % and 0.3 % in the middle and bottom areas. Despite the mean values slightly above 0 %, all the standard deviation bars ended at 0 % as a result of the segregation tendency already reported and discussed in Fig. 8 c and 8 f. Similarly in the R2 condition, the $M_{23}C_6$ fraction moved from 0 % at the top toward a mean value of 0.3 % in the following areas. The inverse evolution of MC and $M_{23}C_6$ fractions along the building direction could suggest a predominant effect of the grain boundaries MC degradation against the direct precipitation of $M_{23}C_6$ during the PBF-EB/M cooling step.

The results of the carbide size evaluation are reported in Fig. 9 b. In

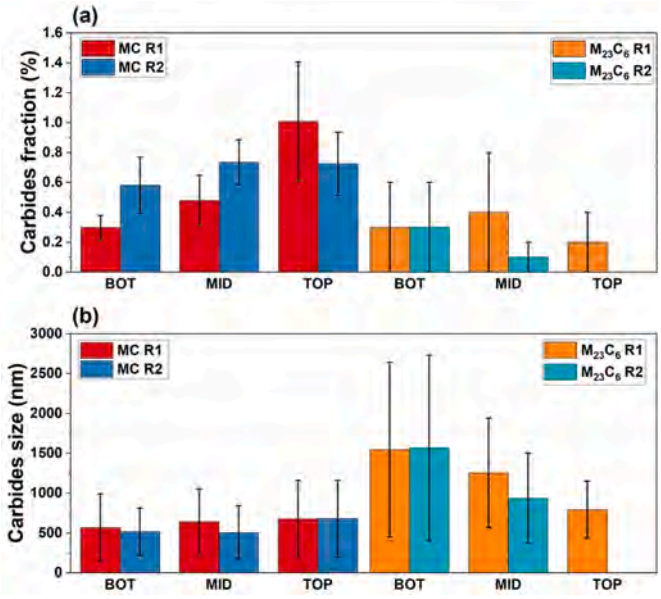

Fig. 9. The fraction (a) and size (b) quantification for the carbides in R1 and R2 conditions. The graphs report the evolution of MC and $M_{23}C_6$ along the building direction.

both R1 and R2 conditions, MC carbides displayed sub-micrometer dimensions between 1 μm and 140 nm without a severe coarsening along the building direction, thus confirming the scenario reported in the literature [26,27,37]. The second type of carbides reported greater dimensions due to their preferentially elongated shape developed along the grain boundaries. Moreover, a coarsening was detected from the top (maximum size 1 μm in R1) to the bottom (max 2.7 μm in R1 and R2). The coarsening could have occurred during the final cooling after the building step, due to the degradation of MC carbides toward $M_{23}C_6$, which was verified to be active up to 700 °C [48,49].

3.4. Effect of microstructural features evolution

GROD, KAM misorientation maps, and LAGBs could be considered an indirect method of evaluating the stresses in a given microstructure. In particular, high misorientation can be associated with high dislocation density, thereby allowing for a correlation with the presence of stresses in the microstructure [50]. To further evaluate the effect of the preheating temperature on the IN738 microstructure, GROD maps coupled with HAGBs/LAGBs and KAM evaluation were performed on R1 and R2 samples in the middle area. Fig. 10 a, b, c, and d represent the GROD, the HAGBs/LAGBs, and the KAM maps and curve of the R1 sample, respectively. The GROD map (Fig. 10 a) revealed the presence of high misorientation values in the AB microstructure with a gradient evolution inside grains. The distorted microstructure resulted in 50 % LAGBs and high KAM misorientation, which was homogeneously distributed throughout the grain structure, as depicted by Fig. 10 b and c. Moreover, the KAM curve (Fig. 10 d) revealed a distribution of misorientation between 0° and 5° with a peak between 0° and 1.5°, pointing out a smooth increase toward a maximum frequency of 25 % at 0.1° misorientation. On the other hand, the R2 sample exhibited a different scenario (Fig. 10 e, f, g, and h). The GROD maps pointed out lower misorientation values than the R1 condition, with a limited gradient among the same grain (Fig. 10 e). Furthermore, the LAGB fraction was measured as 25 % with lower KAM values randomly distributed in a few grains, as visible in Fig. 10 f, and g. The KAM misorientation distribution (Fig. 10 h) showed the peak ranged between 0° and 1° with a sharp increase to 35 % frequency for a misorientation of 0.05°.

By comparing the R1 and R2 conditions, it was evident that both samples underwent the formation of stresses after the building process, as indicated by the GROD maps. This behavior could be attributed to rapid solidification until reaching the preheating temperature. Moreover, the LAGB values (50 % and 25 % for R1 and R2, respectively) and KAM maps could highlight a different dislocation distribution inside grains. By comparing the KAM misorientation curves, the R1 condition pointed out wider areas at higher misorientations. In particular, 90 % of the deformed areas in the R1 condition were below 1°, while in the R2 condition, the same fraction experienced only misorientations below

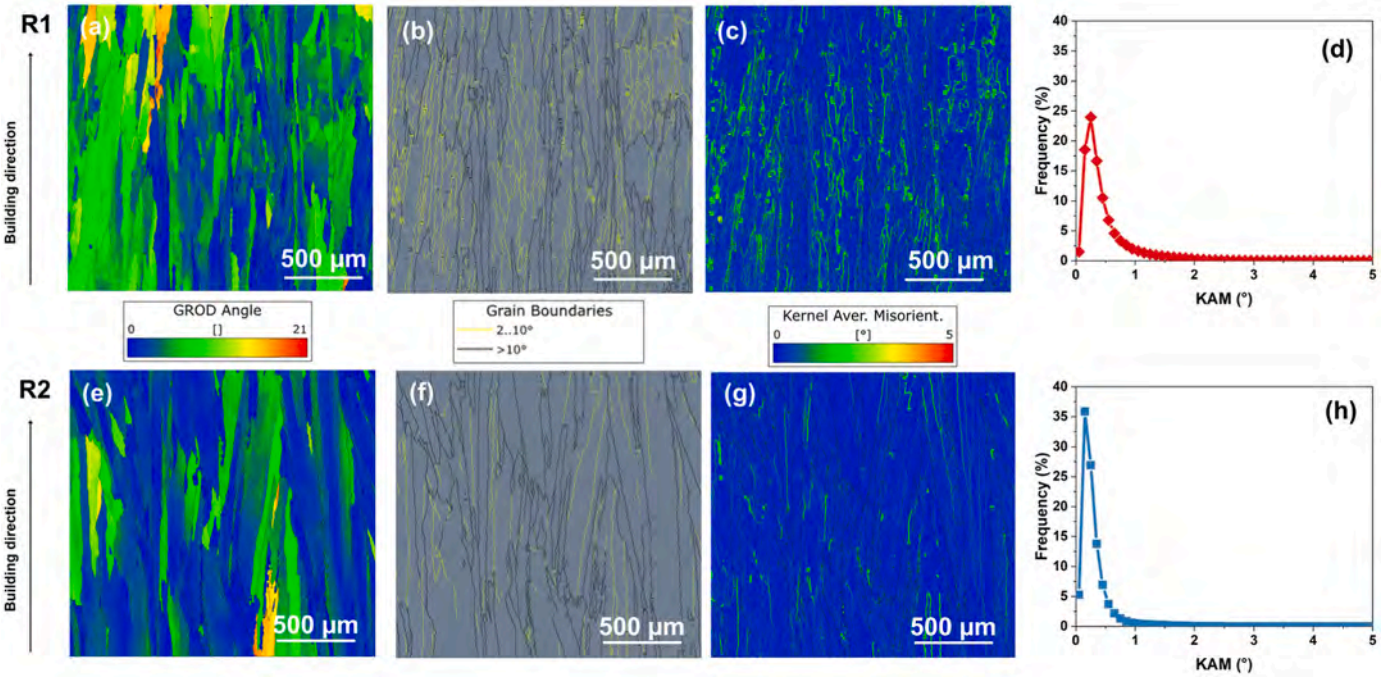

Fig. 10. EBSD analyses on R1 (a–d) and R2 (e–h) samples. The image reports the GROD (a, e) maps, the LAGBs/HAGBs (b with 50 % LAGBs, and f with 25 % LAGBs) evaluation maps, the KAM (c, g) maps, and curves (d, h). The maps were performed along the building direction in the middle zone of the samples investigated.

0.5°. The analysis confirmed a less severe dislocation density in the R2 condition compared to the R1 condition. This behavior could have highlighted an additional contribution that altered the direct correlation between residual stress formation and temperature gradient after the PBF-EB/M production [51]. This contribution could involve the different γ′ evolution. The R1 primary and secondary γ′ particles interacted more efficiently with dislocations formed during the solidification, thus hindering their relief during the soaking within the preheating. This behavior is confirmed by Geddes et al. [10], in which coarse primary γ′ particles turning to a cuboidal shape possessed higher interfacial energy against the γ matrix, thus increasing the interaction efficiency with the dislocation movement. In addition, the size of fine secondary γ′ fitted with the optimal dimension (10 nm–100 nm [10]), thus increasing the hardening effect and resulting in an additional relieving limitation. On the other hand, the monomodal distribution of primary γ' in the R2 sample has exceeded the optimal size (10 nm–100 nm [10]) for maximizing the hardening effect, thus allowing the beginning of the recovery, as confirmed in the literature by Galindo-Nava [52].

3.5. Micro-cracks formation tendency

Fig. 11 reports low-magnification SEM images of the R1 and R2 samples. The R1 sample reported the formation of microcracks along the grain boundaries (Fig. 11 a). In this condition, both types of carbides were found along the crack path, thus suggesting a potential impact on crack initiation. On the contrary, the R2 sample was found crack-free without any micrometrical detachments along the grain boundaries, also where carbide precipitation was observed (Fig. 11 b).

The R1 sample exhibited strong stress development in the γ matrix, which resulted from the combined influence of the building process and the multimodal distribution of γ′. The strain induced at the grain boundaries could have induced the formation of detrimental micro-cracks in this R1 condition [21]. Moreover, the presence of Ta and Cr-rich carbide along the crack path could suggest an influence of the segregation on the crack propagation. According to Luo et al. [53], the segregation of solute elements such as Cr, W, C, B, and P along the grain boundaries plays a relevant role in the formation and evolution of micro-cracks in PBF-EB/M IN738. In particular, the lower cohesion forces induced by the segregation of solute elements led to weaker grain boundaries, reducing their resistance to grain strain and resulting in crack formation. On the other hand, the uniform γ' precipitation in the R2 condition allowed the beginning of the dislocation recovery, reducing the tension acting along the grain boundary. Moreover, the limitation of carbide precipitation could suggest a reduction in solute elements segregation at the grain boundaries, thereby reducing the crack susceptibility of the R2 grain boundaries [53]. The combined effect of lower stresses and segregation resulted in a crack-free microstructure for the R2 sample.

3.6. Microhardness evolution

Fig. 12 shows the Vickers (HV0.2) microhardness evolution along the building direction for the R1 (Fig. 12 a) and R2 (Fig. 12 b) conditions. The differential microstructural evolution given by the preheating conditions allowed an overall increase in HV0.2 values in the R2 condition, compared to the R1 condition. Despite the multimodal precipitation of γ′ in the R1 sample, the coarser particles could have had a major contribution to the HV0.2 values, thus lowering the whole evaluation. Conversely, the monoidal and finer γ' size distribution in R2 led to an increase in HV0.2 values compared to the other condition analyzed.

Furthermore, both R1 and R2 samples underwent an increase in HV0.2 values along the building direction. This behavior could be associated with the preferential coarsening of γ′ particles at the bottom area, due to the higher soaking time at the preheating temperature. According to Hall-Patch theory, larger particles led to a lower microhardness, justifying the property gradient. In their work, Lim et al. [26] reported a similar growth along the building direction, assessing the γ′ fraction and size contribution. Moreover, a tendency to HV0.2 increase from the center to the edges (x direction) was detected in both R1 and R2. This scenario could be correlated with the preferential heat dissipation that could have reduced the γ′ dimensions at the edges, resulting in an HV0.2 increase. Overall, the R2 condition proved to have smoother evolution in both building and x direction as a result of the lower coarsening of γ' particle size, compared to the R1 condition.

4. Conclusions

In the current study, two different preheating conditions were used to investigate the effect of temperature on the precipitation and evolution of phases. The microstructural features and hardness of the as-built IN738 samples were fully characterized. The main results can be summarized as follows.

- The combined use of DSC analyses and Thermo-Calc simulation allowed the identification and selection of two preheating temperature conditions. The 1025 °C one fell in the precipitation temperature ranges of γ′ and $M_{23}C_6$, while the 950 °C one was far from the γ′ and $M_{23}C_6$ maximum precipitation area. The MC precipitation was observed around 1335 °C, far from the preheating temperature ranges, thus making it impossible to optimize this feature.
- To enable preheating at lower temperatures, a new set of process parameters was developed. Despite the different preheating scenarios, the optimization of the melting parameters performed for the R1 (preheated at 1025 °C) and R2 (preheated at 950 °C) conditions led to the production of nearly fully dense samples with residual gas porosity lower than 0.2 %. As expected, the preheating temperature did not alter the sample densification. The grain structure in AB R1 and R2 conditions consisted of columnar grains elongated in the

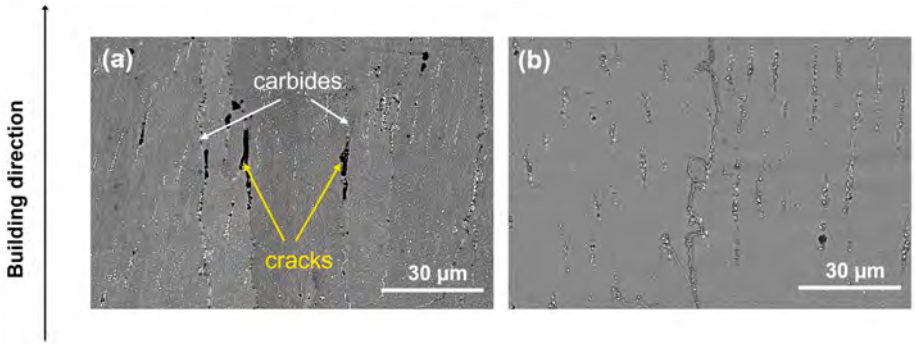

Fig. 11. Cross-section SEM images at low magnification on chemical etched (a) R1 and (b) R2 samples. The images highlight the grain boundary area and the micro-cracks in the R1 condition.

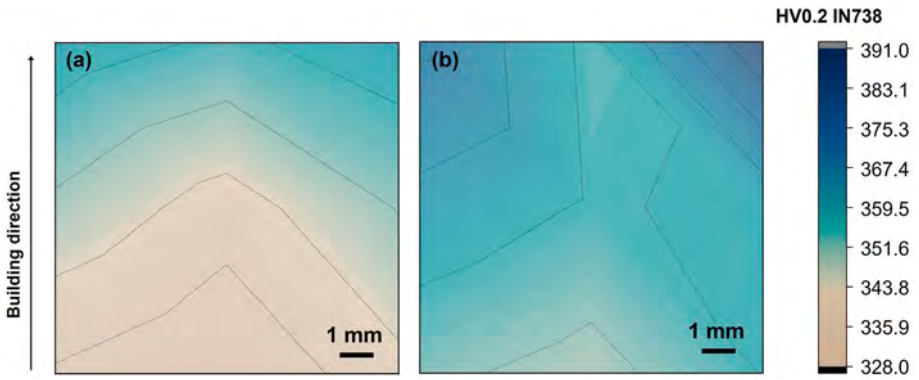

Fig. 12. HV0.2 values on polished cross-section of (a) R1 and (b) R2 samples. The images highlight the microhardness HV0.2 evolution along the building direction.

building direction, following the heat dissipation preferential path. The grain dimension ranges were similar for both conditions, confirming the negligible effect of the preheating temperature on grain coarsening.

- The phase identification step performed through SEM + EDS revealed similarities in terms of the microstructural features. At low magnification, Ta-rich MC carbides and Cr-rich $M_{23}C_6$ were detected in both the R1 and R2 samples by EDS maps. At high magnification, the images focused on the grain area revealed the precipitation of γ' in both the R1 and R2 preheating conditions.
- The use of different preheating temperatures primarily impacted the γ' precipitation, confirming the DSC information. R1 developed a fraction of γ' between 55 % and 62 %, with a multimodal size distribution. The spherical to cuboidal primary γ' particles showed sizes between 1080 nm and 140 nm, while the secondary spherical γ' population was below 89 nm. Conversely, the R2 condition experienced a precipitation of 52 % – 55 % γ' fraction in a monomodal size distribution. Globular γ' particles were observed with diameters between 240 nm and 70 nm. Moreover, the 1025 °C preheating temperature strongly affected the primary γ' coarsening, enhancing the microstructural gradient along the building direction.
- The carbide evolution was influenced to a lesser extent by the preheating conditions. For the R1 condition the carbide fractions ranged from 0.4 % to 1.4 % for MC and 0 % – 0.8 % for $M_{23}C_6$. Similarly, R2 was subjected to the precipitation of MC carbides between 0.2 % and 0.9 %, while the $M_{23}C_6$ fraction was from 0 % to 0.6 %. In both cases, the MC carbides were found in blocky shapes inside the grains and along the grain boundaries, while the $M_{23}C_6$ was preferentially elongated and distributed along the grain boundaries. The two carbide fractions had an opposite evolution along the building direction, thus suggesting the beginning of MC transformation toward $M_{23}C_6$, particularly in the bottom area. The soaking at preheating temperature did not affect the MC carbide coarsening, with sizes ranging between 1000 and 140 nm in the bottom, middle and top areas. On the contrary, the $M_{23}C_6$ went from a maximum of 1 μm length to 2.7 μm, thus confirming the predominant effect of MC transformation.
- The differential precipitation scenario that occurred between the R1 and R2 conditions affected the development of residual stresses. The multimodal distribution of γ' in the R1 condition hindered the beginning of dislocation recovery, resulting in a severely stressed microstructure with higher GROD, LAGB, and KAM values. Moreover, this scenario triggered the formation of sporadic micro-cracks where the carbides acted as crack initiators. On the contrary, the R2 condition developed a more homogeneous γ' precipitation that induced the beginning of an annealing effect with an overall stress reduction. Thanks to this scenario, no cracks were observed in the R2 condition.
- The R2 condition showed overall higher HV0.2 values in the bottom, middle and top areas. In fact, the finer size of the γ' particles compared to the R1 condition allowed an increase in the microhardness values. Moreover, the limited γ' coarsening of the R2 condition along the building direction led to a smoother microhardness gradient evolution. On the contrary, the R1 sample underwent severe microhardness reduction from the top to the bottom areas.

This study proved that a tailored selection of the preheating temperature could affect the microstructural features in the PBF-EB/M process. Lowering the preheating temperature from 1025 °C to 950 °C allowed IN738 samples with finer monomodal size distribution of γ' to be obtained, which reduced the residual stresses developed during the building step and increased the overall microhardness of the alloy.

Declaration of competing interest

The authors declare that they have no known competing financial interests or personal relationships that could have appeared to influence the work reported in this paper.

Acknowledgements

The authors gratefully acknowledge support from the Excellence in Production Research (XPRES) at KTH.

Appendix A

Figure A1 shows examples of SEM images at 20000X (a, b, and c) and 100000X (d, e, and f) focused on γ' in the top, middle and bottom of the R1 sample. Figures A1 a, b, and c better highlight the coarse primary γ' particles, allowing a wider evaluation of their size. On the contrary, high magnification images in Figures A1 d, e, and f focused on the fine secondary γ' particles, thus enabling their size evaluation.

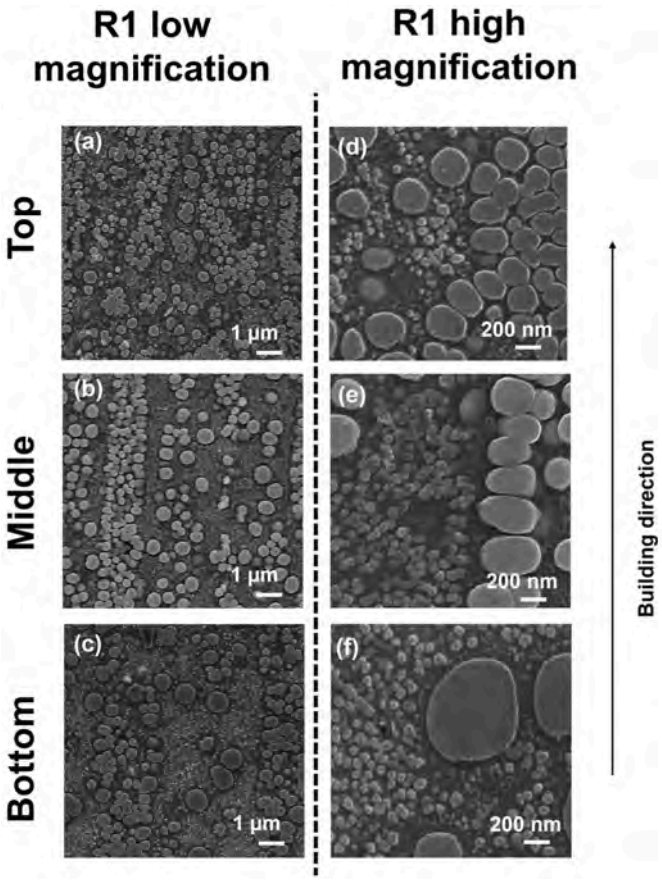

Figure A 1Cross-section SEM images at high (a, b, c) and low (d, e, f) magnification on the chemical etched R1 sample. The images report the γ′ evolution inside the grain area at the top (a, d), the middle (b, e), and the bottom (c, f) zones.

References

[1] Grasso M, Colosimo BM. Process defects and in situ monitoring methods in metal powder bed fusion: a review. Meas Sci Technol 2017;28. https://doi.org/10.1088/1361-6501/aa5c4f.

[2] Milberg J, Sigl M. Electron beam sintering of metal powder. Prod Eng 2008;2:117–22. https://doi.org/10.1007/s11740-008-0088-2.

[3] Cordero ZC, Meyer HM, Nandwana P, Dehoff RR. Powder bed charging during electron-beam additive manufacturing. Acta Mater 2017;124:437–45. https://doi.org/10.1016/j.actamat.2016.11.012.

[4] Sola A, Nouri A. Microstructural porosity in additive manufacturing: the Formation and detection of pores in metal parts fabricated by powder bed fusion. J Adv Manuf Process 2019;1. https://doi.org/10.1002/amp2.10021.

[5] Yan W, Ma W, Shen Y. Powder sintering mechanisms during the pre-heating procedure of electron beam additive manufacturing. Mater Today Commun 2020;25. https://doi.org/10.1016/j.mtcomm.2020.101579.

[6] Körner C. Additive manufacturing of metallic components by selective electron beam melting - a review. Int Mater Rev 2016;61:361–77. https://doi.org/10.1080/09506608.2016.1176289.

[7] Jena A, Atabay SE, Brochu M. Microstructure and mechanical properties of crack-free Inconel 738 fabricated by laser powder bed fusion. Mater Sci Eng, A 2022;850. https://doi.org/10.1016/j.msea.2022.143524.

[8] Chauvet E, Kontis P, Jägle EA, Gault B, Raabe D, Tassin C, Blandin JJ, Dendievel R, Vayre B, Abed S, et al. Hot cracking mechanism affecting a non-weldable Ni-based superalloy produced by selective electron beam melting. Acta Mater 2018;142:82–94. https://doi.org/10.1016/j.actamat.2017.09.047.

[9] Attallah MM, Jennings R, Wang X, Carter LN. Additive manufacturing of Ni-based superalloys: the outstanding issues. MRS Bull 2016;41:758–64. https://doi.org/10.1557/mrs.2016.211.

[10] Geddes Blaine. Superalloys : alloying and performance. ASM International; 2010. ISBN 0615030409.

[11] Reed RC. Superalloys - fundamentals and applications. Cambridge; 2006. p. 33–120. ISBN ISBN-13978-0-521-85904-2.

[12] Ojo OA, Richards NL, Chaturvedi MC. Contribution of constitutional liquation of gamma prime precipitate to weld HAZ cracking of cast Inconel 738 superalloy. Scr Mater 2004;50:641–6. https://doi.org/10.1016/j.scriptamat.2003.11.025.

[13] Ojo, O.A.; Richards, N.L.; Chaturvedi, M.C. On incipient melting during high temperature heat treatment of cast Inconel 738 superalloy;.

[14] Ezugwu EO, Wang ZM, Machado AR. The machinability of nickel-based alloys: a review. J Mater Process Technol 1999;86:1–16.

[15] Akhtar W, Sun J, Sun P, Chen W, Saleem Z. Tool wear mechanisms in the machining of nickel based super-alloys: a review. Front Mech Eng 2014;9:106–19. https://doi.org/10.1007/s11465-014-0301-2.

[16] Fan, W.; Ji, W.; Wang, L.; Zheng, L.; Wang, Y. A review on cutting tool technology in machining of Ni-based superalloys., doi:10.1007/s00170-020-06052-9/ Published.

[17] Messé OMDM, Muñoz-Moreno R, Illston T, Baker S, Stone HJ. Metastable carbides and their impact on recrystallisation in IN738LC processed by selective laser melting. Addit Manuf 2018;22:394–404. https://doi.org/10.1016/j.addma.2018.05.030.

[18] Schulz F, Lindgren K, Xu J, Hryha E. Gamma prime formation in nickel-based superalloy IN738LC manufactured by laser powder bed fusion. Mater Today Commun 2024;38. https://doi.org/10.1016/j.mtcomm.2023.107905.

[19] Zhou W, Zhu G, Wang R, Yang C, Tian Y, Zhang L, Dong A, Wang D, Shu D, Sun B. Inhibition of cracking by grain boundary modification in a non-weldable nickel-based superalloy processed by laser powder bed fusion. Mater Sci Eng 2020;791. https://doi.org/10.1016/j.msea.2020.139745.

[20] Wang H, Zhang X, Wang GB, Shen J, Zhang GQ, Li YP, Yan M. Selective laser melting of the hard-to-weld IN738LC superalloy: efforts to mitigate defects and the resultant microstructural and mechanical properties. J Alloys Compd 2019;807. https://doi.org/10.1016/j.jallcom.2019.151662.

[21] Henderson, M.B.; Arrell, D.; Heobel, M.; Larsson, R.; Marchant, G. Nickel-based superalloy welding practices for industrial gas turbine applications;.

[22] Wang Y, Guo W, Zheng H, Xie Y, Zhang X, Li H, Xu M, Zhang H. Microstructure, crack formation and improvement on nickel-based superalloy fabricated by powder bed fusion. J Alloys Compd 2023;962. https://doi.org/10.1016/j.jallcom.2023.171151.

[23] Kontis P, Chauvet E, Peng Z, He J, da Silva AK, Raabe D, Tassin C, Blandin JJ, Abed S, Dendievel R, et al. Atomic-scale grain boundary engineering to overcome hot-cracking in additively-manufactured superalloys. Acta Mater 2019;177:209–21. https://doi.org/10.1016/j.actamat.2019.07.041.

[24] Haghdadi N, Whitelock E, Lim B, Chen H, Liao X, Babu SS, Ringer SP, Primig S. Multimodal Γ′ precipitation in Inconel-738 Ni-based superalloy during electron-beam powder bed fusion additive manufacturing. J Mater Sci 2020;55:13342–50. https://doi.org/10.1007/s10853-020-04915-w.

[25] Muñiz-Lerma JA, Tian Y, Wang X, Gauvin R, Brochu M. Microstructure evolution of Inconel 738 Fabricated by pulsed laser powder bed fusion. Progress in Additive Manufacturing 2019;4:97–107. https://doi.org/10.1007/s40964-018-0062-2.
[26] Lim B, Chen H, Chen Z, Haghdadi N, Liao X, Primig S, Babu SS, Breen AJ, Ringer SP. Microstructure-property gradients in Ni-based superalloy (Inconel 738) additively manufactured via electron beam powder bed fusion. Addit Manuf 2021; 46. https://doi.org/10.1016/j.addma.2021.102121.
[27] Li Y, Liang X, Peng G, Lin F. Effect of heat treatments on the microstructure and mechanical properties of IN738LC prepared by electron beam powder bed fusion. J Alloys Compd 2022;918. https://doi.org/10.1016/j.jallcom.2022.165807.
[28] Lindwall G, Campbell CE, Lass EA, Zhang F, Stoudt MR, Allen AJ, Levine LE. Simulation of TTT curves for additively manufactured Inconel 625. Metall Mater Trans A Phys Metall Mater Sci 2019;50:457–67. https://doi.org/10.1007/s11661-018-4959-7.
[29] Lin Z, Dabakhsh S, Rashid A. Developing processing windows for powder pre-heating in electron beam melting. J Manuf Process 2022;83:180–91. https://doi.org/10.1016/j.jmapro.2022.08.063.
[30] Zhao X, Dadbakhsh S, Rashid A. Contouring strategies to improve the tensile properties and quality of EBM printed Inconel 625 parts. J Manuf Process 2021;62: 418–29. https://doi.org/10.1016/j.jmapro.2020.12.007.
[31] Wright SI, Nowell MM, Field DP. A review of strain analysis using electron backscatter diffraction. Microsc Microanal 2011;17:316–29. https://doi.org/10.1017/S1431927611000055.
[32] ASTM International. Standard test methods for Vickers hardness and knoop hardness of metallic materials. ASTM; 2023. https://doi.org/10.1520/E0092-23. *E92-23*.
[33] Divya VD, Muñoz-Moreno R, Messé OMDM, Barnard JS, Baker S, Illston T, Stone HJ. Microstructure of selective laser melted CM247LC nickel-based superalloy and its evolution through heat treatment. Mater Char 2016;114:62–74. https://doi.org/10.1016/j.matchar.2016.02.004.
[34] Tancret F. Thermo-calc and dictra simulation of constitutional liquation of gamma prime (Γ′) during welding of Ni base superalloys. Comput Mater Sci 2007;41:13–9. https://doi.org/10.1016/j.commatsci.2007.02.008.
[35] Körner C, Helmer H, Bauereiß A, Singer RF. Tailoring the grain structure of IN718 during selective electron beam melting. In: Proceedings of the MATEC web of conferences, vol. 14. EDP Sciences; 2014.
[36] Kok Y, Tan XP, Wang P, Nai MLS, Loh NH, Liu E, Tor SB. Anisotropy and heterogeneity of microstructure and mechanical properties in metal additive manufacturing: a critical review. Mater Des 2018;139:565–86. https://doi.org/10.1016/j.matdes.2017.11.021.
[37] Adomako NK, Haines M, Haghdadi N, Primig S. On the role of the preheat temperature in electron-beam powder bed fusion processed IN718. Additive Manufacturing Letters 2024;11. https://doi.org/10.1016/j.addlet.2024.100238.
[38] Holt RT, Wallace W. Impurities and trace elements in nickel-base superalloys. Int Met Rev 1976;21:1–24.
[39] Donachie MJ, Donachie SJ. Superalloys. In: ASM international : materials parck. second ed. 2002. OH, USA.
[40] Hu R, Bai G, Li J, Zhang J, Zhang T, Fu H. Precipitation behavior of grain boundary M23C6 and its effect on tensile properties of Ni-Cr-W based superalloy. Mater Sci Eng, A 2012;548:83–8. https://doi.org/10.1016/j.msea.2012.03.092.
[41] Babu SS, Raghavan N, Raplee J, Foster SJ, Frederick C, Haines M, Dinwiddie R, Kirka MK, Plotkowski A, Lee Y, et al. Additive manufacturing of nickel superalloys: opportunities for innovation and challenges related to qualification. Metall Mater Trans A Phys Metall Mater Sci 2018;49:3764–80. https://doi.org/10.1007/s11661-018-4702-4.
[42] Radis R, Schaffer M, Albu M, Kothleitner G, Pölt P, Kozeschnik E. Multimodal size distributions of Γ′ precipitates during continuous cooling of UDIMET 720 Li. Acta Mater 2009;57:5739–47. https://doi.org/10.1016/j.actamat.2009.08.002.
[43] Elorz Pero-Sanz, Antonio J. Solidification and solid-state transformations of metals and alloys. Elsevier; 2017. ISBN 9780128126073.
[44] Ge L, Zhang XN, Guo WG, Dong P, Yu T, Liu CP, Yuan Y, Wang CY, Zhang Z. The coarsening behavior of Γ′ phases in Ni-Al binary model single crystal superalloy at 1000 °C. J Alloys Compd 2022;911. https://doi.org/10.1016/j.jallcom.2022.164989.
[45] Yang J, Zheng Q, Sun X, Guan H, Hu Z. Relative stability of carbides and their effects on the properties of K465 superalloy. Mater Sci Eng, A 2006;429:341–7. https://doi.org/10.1016/j.msea.2006.05.091.
[46] Choi BG, Kim IS, Kim DH, Jo CY. Temperature dependence of MC decomposition behavior in Ni-base superalloy GTD 111. Mater Sci Eng, A 2008;478:329–35. https://doi.org/10.1016/j.msea.2007.06.010.
[47] Zhou W, Tian Y, Wei D, Tan Q, Kong D, Luo H, Huang W, Zhu G, Shu D, Mi J, et al. Effects of heat treatments on the microstructure and tensile properties of IN738 superalloy with high carbon content fabricated via laser powder bed fusion. J Alloys Compd 2023;953. https://doi.org/10.1016/j.jallcom.2023.170110.
[48] Zhang L, Li Y, Zhang Q, Zhang S. Microstructure evolution, phase transformation and mechanical properties of IN738 superalloy fabricated by selective laser melting under different heat treatments. Mater Sci Eng, A 2022;844. https://doi.org/10.1016/j.msea.2022.142947.
[49] Mastrometteo F, Giannozzi M, Pignone G-N, Bardi FU. ASME turbo expo 2004. In: Proceedings of the he coarsening kinetic of γ' particles in NICKEL-BASED superalloys during aging at high temperatures; 2004.
[50] Guglielmi PO, Ziehmer M, Lilleodden ET. On a novel strain indicator based on uncorrelated misorientation angles for correlating dislocation density to local strength. Acta Mater 2018;150:195–205. https://doi.org/10.1016/j.actamat.2018.03.009.
[51] Li Y, Long H, Wei B, Zhou J, Lin F. Multiple preheating processes for suppressing liquefaction cracks in IN738LC superalloy fabricated by electron beam powder bed fusion (EB-PBF). Materials 2024;17. https://doi.org/10.3390/ma17225667.
[52] Galindo-Nava EI, Connor LD, Rae CMF. On the prediction of the yield stress of unimodal and multimodal γ' nickel-base superalloys. Acta Mater 2015;98:377–90. https://doi.org/10.1016/j.actamat.2015.07.048.
[53] Luo M, Rielli VV, Farabi E, Liao X, Ringer SP, Haghdadi N, Primig S. Grain boundary crystallography and segregation in Ni-based superalloy INC738 manufactured by electron-beam powder bed fusion in as-built and annealed conditions. Mater Char 2024;217. https://doi.org/10.1016/j.matchar.2024.114421.